Erosion mechanisms of debris flow on the sediment bed

Erosion mechanisms of debris flow on the sediment bed

Hongchao Zheng[1], Zhenming Shi[1], Songbo Yu[1]*, Xuanmei Fan[2]*, Kevin J Hanley[3], Shijin Feng[1]

[1]Key Laboratory of Geotechnical and Underground Engineering of the Ministry of Education, and Department of Geotechnical Engineering, College of Civil Engineering, Tongji University, China

[2]State Key Laboratory of Geohazard Prevention and Geoenvironment Protection, Chengdu University of Technology, China

[3]School of Engineering, Institute for Infrastructure and Environment, The University of Edinburgh, United Kingdom

Corresponding author: Songbo Yu, yusongbo@tongji.edu.cn; Xuanmei Fan, fanxuanmei1@gmail.com

Key Points:

(1) Flow depth and velocity over a coarse-grained sediment (d_{50} = 2.4 mm) and a widely graded sediment (d_{50} = 0.9 mm) differed substantially

(2) The coarse-grained bed sediment was eroded by mass movement while the widely graded bed sediment was progressively scoured

(3) The interaction between the overlying flow and sediment bed controlled the erosion pattern

Abstract

Debris flows are common geological hazards in mountainous regions worldwide. The scale of debris flows can be significantly enhanced by basal erosion and bank collapse in the transportation process, resulting in an increase in casualties and property losses. However, the mechanisms of this growth are largely unclear. Here, we conduct a series of experiments to investigate the erosion of two different bed sediments (coarse-grained and widely graded) by released flows with three different densities and two different volumes. The erosion mechanisms of bed sediments are revealed by comparing detailed sensor data for flow level, pore pressure and total normal stress. A flow nose develops on the coarse-grained bed sediment, resulting in a high flow depth and low velocity, while a tabular flow develops on the widely graded bed sediment, leading to a low flow depth and high velocity. The mean erosion rates of the coarse-grained bed sediment are generally higher than those of the widely graded bed sediment due to significant pore pressure developed in coarse-grained bed sediment. The feedback effect of bed sediment on the erosion process strongly influences the flow depth and velocity, which in turn affects the mean erosion rate of bed sediment. The interaction between the overlying flow and sediment bed controls the erosion pattern: coarse-grained bed sediment is eroded by a layer of mass movement whereas widely graded bed sediment is progressively scoured. The interaction between debris flow and bed sediment during erosion is principally attributed to pore-pressure transmission.

1. Introduction

Debris flows generally develop in steep valleys when loose debris and landslides initiate due to rainfall or snow melting [*Costa,* 1988; *Iverson,* 1997; *Suwa et al.,* 2009; *Pudasaini,* 2012]. In recent years, the occurrence and scale of debris flows have increased significantly due to frequent earthquakes, severe wildfires, volcanic eruptions, and climate change [e.g., *Houghton et al.,* 2001; *Pierce et al.,* 2004; *Dowling and Santi,* 2014; *Stoffel et al.,* 2014; *Gregoretti et al.,* 2018; *Fan et al.,* 2019]. Debris flows can cover floodplains, block rivers and deteriorate the regional ecological environment in the transportation processes [*Takahashi,* 2007; *Shi et al.,* 2018; *Zheng et al.,* 2021].

Debris flows can be increased in size by basal erosion and side collapse during the flow process, enhancing their run-out distances and hazardous impacts [e.g., *Pierson,* 1980; *Berti et al.,* 1999; *Gregoretti,* 2000; *Wang et al.,* 2003; *Breien et al.,* 2008; *Guthrie et al.,* 2010; *Reid et al.,* 2016; *Simoni et al.,* 2020]. Some debris flows grow by several orders of magnitude before deposition on the alluvial fan downstream

[*Jakob et al.,* 2005; *Santi et al.,* 2008; *Navratil et al.,* 2013; *Theule et al.,* 2015]. By contrast, other debris flows have been observed to barely erode [*Pérez,* 2001]. The mechanisms that govern the growth of debris flows are still unclear, hampering efforts to assess natural hazards in debris flow-prone areas [*Mangeney,* 2011; *Pudasaini and Fischer,* 2020a].

Different experimental research studies have been conducted to investigate the influences of flow variables on the erosion potential. The experimental results indicate that erosion potential has a positive correlation with flow velocity [e.g., *Iverson,* 2012], flow depth [e.g., *Schürch et al.,* 2011; *Berger et al.,* 2010], triggering liquid discharge [e.g., *Lanzoni et al.,* 2017; *Simoni et al.,* 2020], flow volume [e.g., *Chen et al.,* 2005], bed slope [e.g., *Conway et al.,* 2010; *Theule et al.,* 2015], shear stress [e.g., *Schürch et al.,* 2011; *Berger et al.,* 2011; *Han et al.,* 2015; *Zheng et al.,* 2018] and grain collisional stress [e.g., *Hsu et al.,* 2008, *Yohannes et al.,* 2012]. Currently, the research of erosion mechanisms is focused on the invasive overlying flow [*de Haas and van Woerkom,* 2016]. The feedback effect of the underlying bed sediment on the erosion process has rarely been studied [*Pudasaini and Fischer,* 2020a; *Pudasaini and Krautblatter,* 2021]. In reality, debris-flow erosion depends on the interaction between the flow and bed sediment. This interaction process has been successfully simulated by a fully mechanical model of erosion-induced growth of volume and mobility [*Pudasaini and Fischer,* 2020a; *Pudasaini and Krautblatter,* 2021]. Experimental results indicate that the water content of the bed sediment affects debris-flow propagation during erosion [*Iverson et al.,* 2011]. However, the growth process of debris flows on bed sediments of different grain compositions has rarely been explored.

The erosion potential is affected by the debris-flow density due to the combined consequence of basal shear stress and debris-flow solid concentration [*Pudasaini and Fischer,* 2020a]. For the former, erosion potential is commonly considered to increase with the debris-flow density as a result of a larger basal shear stress [e.g., *Quan Luna et al.,* 2012; *Chen and Zhang,* 2015] and grain collisional stress [*Stock and Dietrich,* 2006; *Hsu et al.,* 2008]. For the latter, the quantity of eroded sediments transported by debris flow can be reduced with a larger debris-flow solid concentration [*Hungr et al.,* 2005]. In laboratory experiments, the erosion rate was observed to increase with the increase of flow density up to 1700 kg/m^3, and thereafter decrease with flow density [*Rickenmann et al.,* 2003]. This trend is possibly consistent with the hypothesis that an equilibrium volumetric sediment concentration is reached when the erodible bed is eroded by a flow above [*Takahashi et al.,* 1992]. In addition, a debris flow can be within the frictional, collisional or viscous regime at the same flow density and the

erosion rate of bed sediment can be affected by the dominant stress in different flow regimes [*Lanzoni et al.,* 2017].

Analyses of the erosion process in field and laboratory experiments have demonstrated that erosion beneath debris flows generally occurs by incorporating the bed sediments by mass movement and progressive scour [*Takahashi,* 2007; *Berger et al.,* 2011; *Iverson et al.,* 2011; *McCoy et al.,* 2012; *de Haas and van Woerkom,* 2016]. These studies have additionally shown that erosion rates are sensitive to characteristics of flow behavior such as flow depth and velocity as well as pore pressures developed in bed sediment as it is overridden. However, the correlation between the erosion rate and the erosion pattern of mass movement and progressive scour is unknown.

We conducted a series of erosion experiments under closely controlled conditions to analyze the feedback effects of bed sediments on flow characteristics such as flow depth and velocity, investigate the difference in erosion rates, and discern the erosion patterns. Following the mechanical model by *Pudasaini and Fischer* [2020a] and *Pudasaini and Krautblatter* [2021], a hypothesis is proposed that the erosion of bed sediment strongly influences flow behavior, which in turn affects their erosion pattern and erosion rate. By observing how the type of bed sediment controls the erosion patterns, we were able to reveal the interaction between a debris flow and a sediment bed during erosion.

The structure of this paper is as follows. First, experimental flume setup, debris-flow compositions and the measurement and data reduction techniques are described. Then, we present observations of the flow characteristics, erosion patterns and mean erosion rate. Based on these observations, the erosion mechanisms are revealed from the interactions between each flow and the underlying sediment bed. Additionally, the effects of pore pressure, flow volume and flow density on the mean erosion rate are analyzed. Finally, we discuss the erosion pattern and mobility and show briefly how the experimental results may be translated to natural systems in terms of scaling.

2. Materials and Methods

2.1. Experimental Setup

The experimental apparatus consisted of a transport platform, mixing tank and straight-slope flume (Figure 1 and Supplementary Figure S1). The mixing tank with a volume of 0.7 m^3 was used to store and mix the flow. The flume was fixed at an angle α of 18° to the horizontal plane based on Hsiaolin debris flow [*Dong et al.,* 2011] and had a height of 0.4 m, a width of 0.3 m and a length of 8.0 m. The flume sidewalls were made of transparent tempered glass, allowing the erosion process to be observed.

The bottom of the flume was patterned steel roughened by small bulges with a roughness height of 1.6 mm to simulate natural channel roughness.

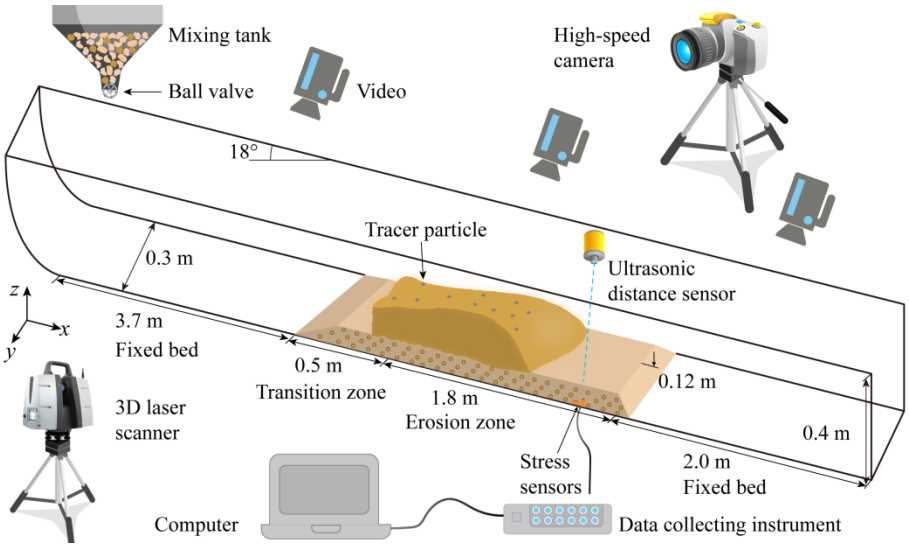

Figure 1. Schematic diagram of experimental apparatus.

Various instruments were used for investigating the erosion process of debris flow (Figure 1). Three video cameras (GZ-R10BAC, JVC, 1920 x 1080 pixel), each with a sampling frequency of 25 Hz, recorded the movement of debris flows from the top of the flume. A high-speed camera (i-SPEED7, iX Cameras, sample frequency 179 Hz) in the cross-stream direction was used to observe the erosion process. A 3D laser scanner (ScanStation P40, Leica, measurement accuracy 1.2 mm+10 ppm) was employed to obtain the thicknesses of the sediment bed before and after the passage of debris flows. At x = 5.8 m we deployed arrays of electronic sensors to measure the pore pressure p, total normal stress σ and flow level h with a sample frequency of 100 Hz. The pore-pressure sensor was saturated and accommodated in a cavity of the bed, filled with water and covered with sand (1–2 mm). Calibrations of these sensors using static water pressures yielded regression line slopes that were both linear (determination coefficient $R^2 > 0.99$) and reproducible. We used an ultrasonic sensor (U-GAGE Banner, T30U) with a precision of 1 mm to measure the flow surface level. This sensor was hung above the pore-pressure and stress sensors and calibrated with a steel ruler by measuring the distance from the horizontal ground.

2.2. Material Compositions

The grain composition of the released flows was based on Hsiaolin debris flow, as shown in Figure 2 [*Dong et al.,* 2011]. The fine component (0.001–0.01 mm) used to prepare the slurry was hydrous kaolin. 78.3% of the fine particles by volume had a grain size less than 2 μm, and 99.8% less than 10 μm. The debris composition (0.01–5 mm) was created by mixing silt, sand and gravel.

Based on the grain composition of the released flow, the grading curves of widely graded bed sediment (WBS) and coarse-grained bed sediment (CBS) were derived. The median grain sizes d_{50} of the WBS and CBS were 0.9 mm and 2.4 mm, respectively. The size distribution of the WBS was the same as that of the debris flow omitting the fine component. The CBS consisted of coarse sand (1–2 mm) and gravel (2–5 mm).

Three types of loose sediments were classified by the catchment lithology based on 1728 debris-flow cases in the Susa Valley [*Tiranti et al.,* 2008]. The sediment generated by igneous or coarse-grain metamorphic rocks had a size distribution within the range 0.01–20 mm and median size d_{50} of 0.8–2.7 mm which was similar to WBS in our experiments (Table 1). The sediment produced by massive carbonate rocks contained more than 80% coarse grains larger than 1 mm and had a d_{50} of 2.1–7.8 mm which was similar to our CBS.

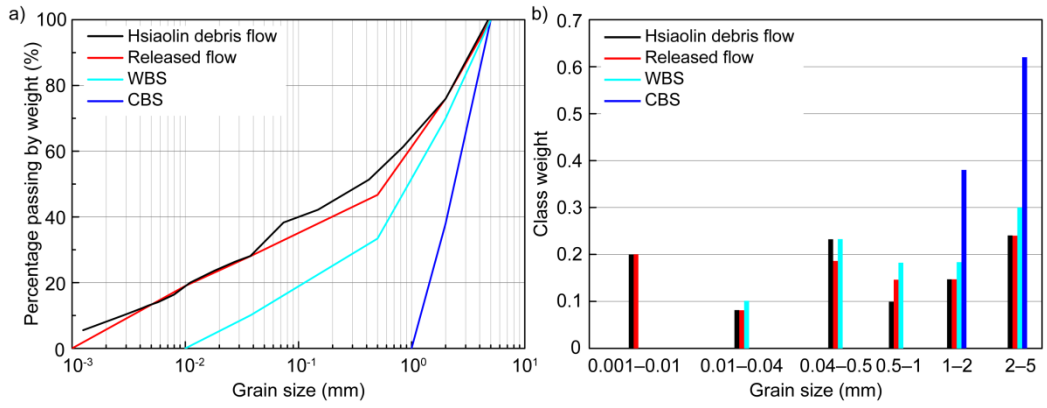

Figure 2. Grain compositions of the Hsiaolin debris flow, released flow, widely graded bed sediment (WBS) and coarse-grained bed sediment (CBS): a, Cumulative particle-size distribution; b, frequency distribution.

Geotechnical properties of bed sediments were measured. From constant-head permeameter tests [e.g., *Iverson et al.*, 2010], the saturated permeability coefficients k of the WBS and CBS at the same dry density in the process of erosion were 0.07 cm/s and 2.76 cm/s, respectively (Table 1). Considering the large displacement and deformation of bed sediment in the erosion process, we conducted ring shear tests (GCTS, SRS-150) to obtain the shear strengths (cohesions c and internal friction angles φ).

Table 1. Geotechnical properties of widely graded bed sediment (WBS) and coarse-grained bed sediment (CBS)

Sediment type	Grain size (mm)	d_{50} (mm)	k (cm/s)	c (Pa)	φ (°)
WBS	0.01–5	0.9	0.07	0	27.2
CBS	1–5	2.4	2.76	0	33.3

2.3. Data Collection

We used three video cameras and a steel tape to infer the flow-front position and front velocity. The average velocity $\bar{v}$ of flow on the sediment bed was obtained from the motion of black-tagged particles on video recordings. One flow sediment sample was manually collected with a measuring glass when the debris flow front just reached x = 4.2 m. This sample was dried in an oven to calculate the flow-front density. The height of flow at the flow front was obtained using the steel tape and snapshots taken by the high-speed camera. The method adopted for processing the digital data produced by the electronic sensors is described by *Iverson et al.* [2010].

We measured bed-sediment thicknesses before and after passage of the released flows by using a 3D laser scanner. To avoid the shadow of the flume sidewalls, three scans were conducted in different locations for every scanning operation and these point clouds (more than a million points) were incorporated together using three targets in black and white. As shown in Figure 3, point clouds of the bed sediment were first extracted from the overall site. Then, the point clouds before and after erosion were combined by adjusting the spatial coordinate system. The point clouds were processed with MATLAB (The MathWorks, version R2018a) using natural neighbor interpolation to a gridded DEM (Digital Elevation Model) of bed sediment [*Boreggio et al.,* 2018]. The erosion distribution of bed sediment was determined by subtracting initial and final elevations. Finally, the total erosion volume V_b was calculated by adding all the volumes of net bed erosion. The spatial morphology of the bed sediment after erosion was also captured.

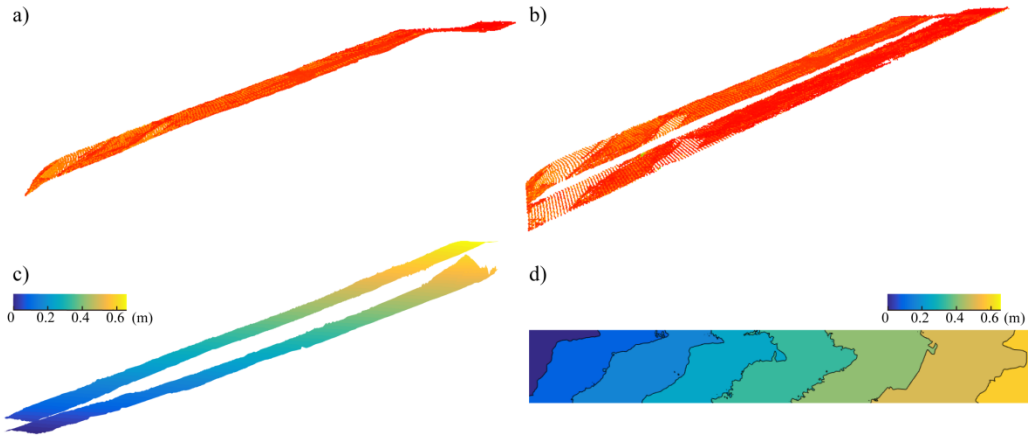

Figure 3. Data extraction of bed sediment: (a) combined point clouds of three scans. The color of the point clouds does not represent any material property. (b) point clouds of bed sediment before and after erosion; (c) gridded data of bed sediment before and after erosion; (d) contour map of bed sediment after erosion. Panels (a), (b) and (c) are the side views of bed sediment and panel (d) is the plan view of bed sediment after erosion.

2.4. Experiments and Procedure

The experimental procedure involved each released flow moving downward on the fixed bed upstream, then eroding the sediment bed and flowing across the fixed bed downstream (Figures 1 and S1). The relevant parameters varied in the experiments were the released flow density ρ_0, flow volume V_0, and bed sediment type. In total, 16 experiments were performed, as shown in Table 2. To account for the effects of natural variability, some experiments were repeated twice which are identified with an asterisk.

After a released flow reached the sediment bed, the flow-front velocity first decreased due to the interaction of the flow with the sediment bed. The sediment bed was divided into transition and erosion zones (Figure 1). According to video recordings, the transition zone was determined to be located between x = 3.7 m and 4.2 m (x = 0 denotes the flow release location), considering that the flow-front velocity remained stable after this zone. The erosion zone was located between x = 4.2 m and 6.0 m.

The released flow densities from the mixing tank were 1000 kg/m^3 (water), 1500 kg/m^3 or 1700 kg/m^3 for producing debris flows with different densities. After the released flows of density 1000 kg/m^3 moved over the transition zone (x = 4.2 m), the bulk densities of the debris flows at the flow front increased to 1470–1560 kg/m^3. For the released flows of densities 1500 or 1700 kg/m^3, the flow-front bulk densities of the debris flows were 1590–1730 or 1790–1870 kg/m^3, respectively, downstream of the transition zone. The discussion of erosion in the following sections is limited to erosion in the erosion zone.

The volumes of the released flows V_0 were 0.04 m^3 or 0.07 m^3. The released flows were prepared as follows. First, the masses of debris grains and water in each flow were calculated according to the required flow density and flow volume. Then, the debris material was lifted onto the transport platform by a winch and poured into the mixing tank (Figure S1). Water was injected into the mixing tank. Finally, the water and debris were adequately mixed using a portable rotary mixer before releasing the flow.

The CBS and WBS were prepared according to the corresponding grain composition (Figure 2). The uniform bed layer averaged 12 cm in thickness and covered the surface of the fixed flume bed. The sediment bed was formed by depositing debris material in layers of approximately 4 cm thickness on the surface of the flume slope. After each layer was deposited, it was uniformly compacted by slightly tapping with a steel trowel to obtain a loose packing. Samples of each sediment lining the flume initially had dry densities of 1500±50 kg/m^3. The bed

sediments were moistened as much as possible by spraying water until considerable water was seeping out. The mass water content w was 0.11±0.02 (saturation degree θ = 0.37±0.07) for the WBS and 0.06±0.02 (θ = 0.20±0.07) for the CBS due to the difference in their water retention capacities.

Table 2. Characteristics of the different experiments

Experiment	V_0 (m^3)	ρ_0 (kg/m^3)	Bed type
C1	0.04	1000	CBS
C2	0.07	1000	CBS
C2*	0.07	1000	CBS
C3	0.04	1500	CBS
C4	0.07	1500	CBS
C4*	0.07	1500	CBS
C5	0.04	1700	CBS
C6	0.07	1700	CBS
W1	0.04	1000	WBS
W2	0.07	1000	WBS
W2*	0.07	1000	WBS
W3	0.04	1500	WBS
W4	0.07	1500	WBS
W4*	0.07	1500	WBS
W5	0.04	1700	WBS
W6	0.07	1700	WBS

3. Results and Analysis

In this section, the erosion process of flows on the CBS and WBS is first presented with reference to flow depth, velocity, mean erosion rate and erosion pattern. Then, the erosion mechanism is discussed with the aim of clarifying the flow behavior on bed sediment.

3.1. Erosion Process

As documented by video recordings, following abrupt opening of the ball valve, the flow fell into the flume and accelerated within the first 2.0 meters (Figure 4). Then, shallow flows propagated downstream at a uniform velocity before encountering the sediment bed. The flow-front paths were clearly divided into two groups based on the bed typology when solid–liquid mixtures were flowing over the wet sediment beds. Flow-front velocities slightly decreased in the transition zone of a WBS (W1–W6), after which these flows maintained their speeds to the end of the flume. By contrast, flow-front velocities significantly decreased in the transition zone of a CBS (C1–C6) and these velocities remained nearly unchanged in the erosion zone (x = 4.2–6.0 m).

Flow C1 in particular had a very low flow-front velocity and it took longer to pass through the flume than any other flow.

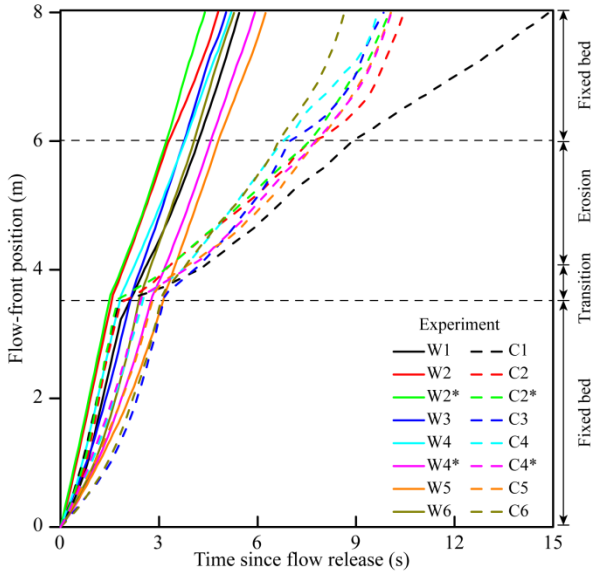

Figure 4. Measured positions of flow fronts in experiments. The solid and dashed lines depict the erosion experiments on the WBS (W1–W6) and CBS (C1–C6), respectively. The repeated experiments are identified with an asterisk.

Significant differences occurred in the erosion process of debris flows on the CBS and WBS. As shown in Figures 5a–5c, a high flow nose developed when the debris flow moved over the CBS. The flow velocity in the flow nose was lower than the velocity of the finer-grained and more dilute material behind the flow nose. As a consequence, the flow nose moved forwards, pushed by the following flow body. This phase separation between the coarse grains and slurry material is expected from the mechanical phase separation model proposed by *Pudasaini and Fischer* [2020b]. The nose grew in size as additional sediment grains were incorporated into the flow front. Coarse grains just behind the nose were recirculated, while those reaching the nose were overrun and deposited (Figure S2), resulting in a steady flow nose. The bed sediment behind the nose was eroded in the form of a layer of mass movement. For flows C3 and C5, part of the flow nose was deposited on the surface of the bed sediment whereas the flow nose was transitorily deposited and then carried away by the subsequent flow body for other flows (Figure 6). Frictional behavior was observed at the snout in the absence of fluid. The height of the flow nose ranged from 4.1 cm to 8.9 cm increasing with the volume of the released flow.

A tabular flow developed when the released flows moved on the WBS (Figures 5d–5f and S3). The height of tabular flows ranged from 2.0 cm to 3.2 cm: lower than the flow noses on the CBS. Flow height and velocity from the flow front to flow body did not display a significant change. The schematic diagram of the tabular flow is

shown in Figure S4. The tabular flow initially covered the surface of the bed sediment and then occupied only a fraction of the flume width with a lower height. A sheet of viscous slurry was deposited on the surface of the WBS for flows W5 and W6. No deposition phenomena were observed for the other flows (Figure S5). In general, the heights of tabular flows slightly increased with increased flow-front density or flow volume.

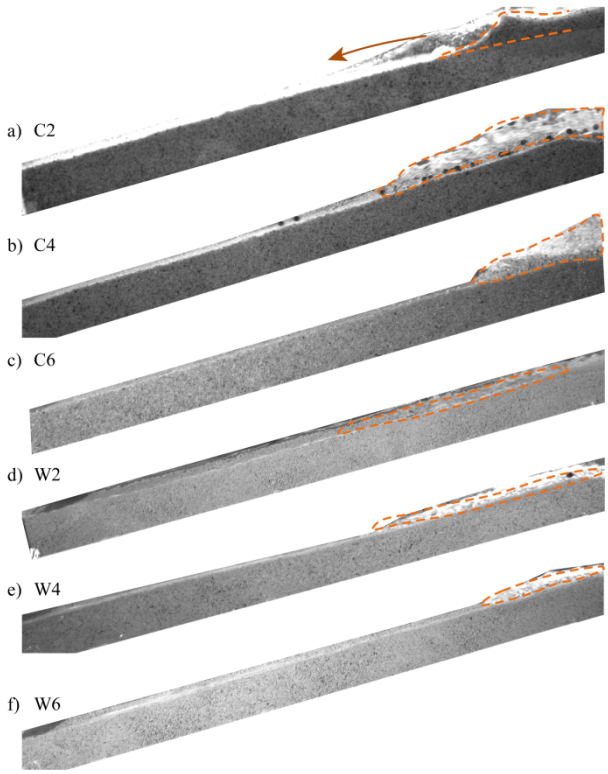

Figure 5. Snapshots of debris-flow erosion on the sediment bed of experiments C2, C4, C6 and W2, W4, W6. Debris flow is located in the orange dashed box and the sediment bed is at the bottom. The black particles above the sediment bed are tracer particles.

The average flow velocity in the experimental runs on the CBS was in the range 0.41–0.66 m/s. Tabular flows had significantly higher flow velocities in the range 1.17–1.48 m/s. The reductions in velocity on the CBS were more than 50%, whereas those on the WBS were close to 25%. Conversely, the differences in velocity reduction between debris flows of different densities and volumes on the same erodible bed were less than 7%.

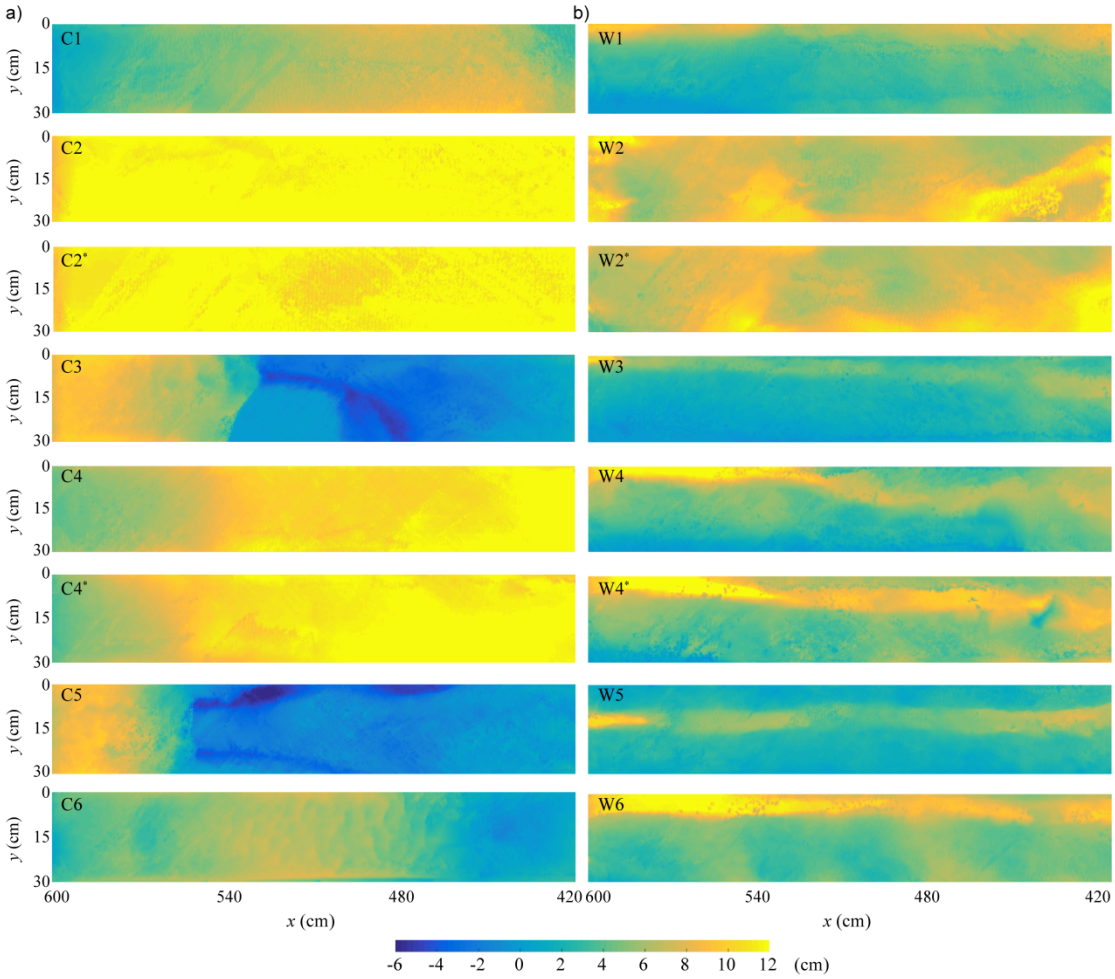

Figure 6. Erosion distribution on the erosion zone of (a) CBS (C1–C6) and (b) WBS (W1–W6). Flows propagate from right to left and thus the scales increase from right to left in the abscissas. Positive values represent flow erosion and negative values represent flow deposition. Deposition in our experimental debris flows is treated as negative erosion in accordance with *Berger et al.* [2010] and *Iverson* [2012]. The distribution of erosion depth was similar for repeated experiments; the volume difference of bed-sediment erosion was less than 9% by comparing C2 and C2*, C4 and C4*, W2 and W2*, W4 and W4*.

The distribution of erosion depth displayed high consistency on the same sediment beds, regardless of released flow volume and flow density (Figure 6). The erosion depths of the CBS were relatively uniform in cross-sections of the bed sediment. By contrast, a strip of channelized erosion along the direction of flow movement was formed on the WBS.

The erosion pattern of debris flows can be inferred from the distribution of erosion depth. The flow nose propagated downstream, pushed by the following flow body. The bed sediment behind the flow nose was eroded by a layer of mass movement (Figure S2) [*Iverson et al.,* 2011; *McGuire et al.,* 2017]. The erosion depth had a relatively uniform distribution in the cross-sectional direction as a result of

erosion in the layer of mass movement. Surficial sediment on the WBS was eroded by progressively scouring bed sediments (Figure S3). Subsequent flow moved and eroded within a fraction of the flume width with a lower height. Eventually, an area of channelized erosion occurred along the erodible bed. The curving channel could be on the left, right or in the middle of the sediment bed. The stochastic nature of channelized erosion as regards its location and trajectory may be ascribed to slightly uneven bed surfaces during the preparation of bed sediment.

As shown in Figure 7, erosion depth at x = 5.8 m was relatively uniformly distributed in the cross-section of the CBS. The standard deviation of erosion depth was within the range 0.24–0.67 cm. Conversely, the erosion depth displayed an uneven distribution on the WBS with a standard deviation in the interval 0.76–4.41 cm. The erosion depth decreased with the increase of flow-front density on the CBS which was not observed on the WBS. The WBS was partially incorporated into the debris flow. However, the CBS was nearly completely carried away by flows C2 and C2*. This is similar to supply-limited erosion by a natural debris flow [*Abancó and Hürlimann,* 2014].

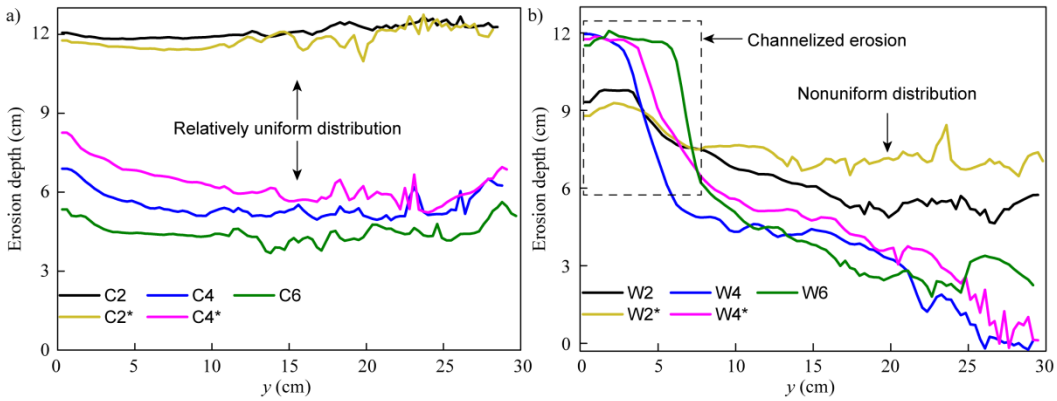

Figure 7. Erosion depth in the cross-section at x = 5.8 m: (a) flows C2, C2*, C4, C4* and C6; (b) flows W2, W2*, W4, W4* and W6.

To evaluate the growth rate quantitatively during debris-flow erosion, we calculated the mean erosion rate q as

$$q = \frac{V_b}{t_e BL} \tag{1}$$

where V_b is the erosion volume, t_e is the erosion time, and B and L are the width (0.3 m) and length (1.8 m) of the sediment bed, respectively. q denotes the value averaged over the entire flow duration and over the entire erodible bed area. The erosion volume V_b and q are summarized in Table 3. Several sources may have contributed to error in this process. The maximum volume error was less than 1% when the point clouds of bed sediment were separated from flume sidewalls with a grid size of 3 mm.

The maximum cumulative error of erosion time t was 0.08 s by using the 0.04 s resolution of video recordings. We determined error bars for q by propagating the errors in V_b and t_e.

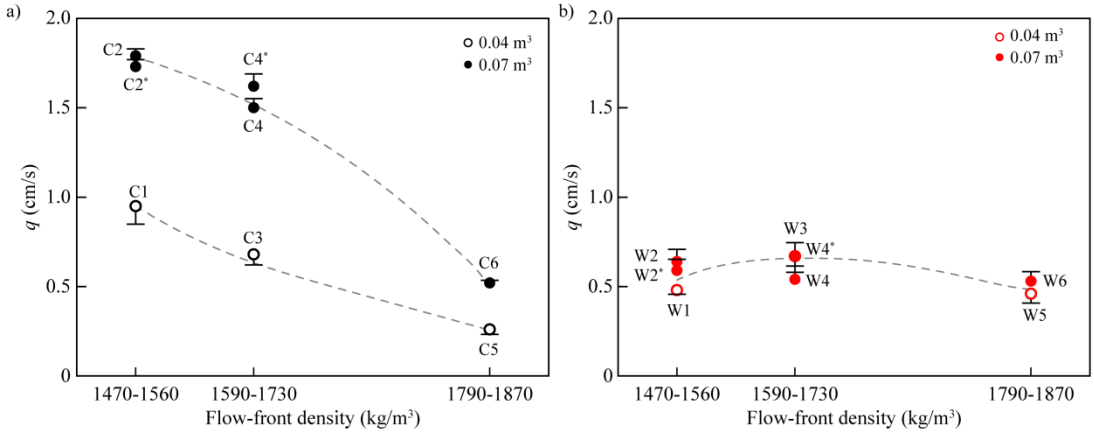

Figure 8. Mean erosion rates of flows on (a) CBS and (b) WBS.

As shown in Figure 8, the CBS generally had a greater mean erosion rate q than the WBS for the same released flow except for flow C5, although the shear strength of the CBS was higher than that of the WBS. For example, q of flows C2 and C2* were greater than 1.7 cm/s, which were nearly 3 times those of flows W2 and W2* (close to 0.60 cm/s from Table 3). q decreased with the increase of flow-front density for the CBS. By contrast, q increased first and then decreased with increasing flow-front density for the WBS. In addition, q increased with the released flow volume for the CBS whereas q remained almost the same for the WBS. The high consistency in the erosion pattern and repeatability of the results suggests that the trends obtained here are applicable for understanding the effects of bed sediment on the erosion process of debris flow.

Table 3 Erosion variables of debris flows in the erosion zone

Experiment	V_b (10^{-2} m^3)	$\bar{v}$ (m/s)	q (cm/s)
C1	2.87	0.41	0.95
C2	5.88	0.46	1.79
C2*	5.62	0.45	1.73
C3	0.88	0.66	0.68
C4	4.61	0.62	1.50
C4*	5.05	0.48	1.62
C5	0.41	0.48	0.26
C6	2.05	0.66	0.53
W1	1.97	1.17	0.48
W2	3.91	1.42	0.64

W2*	3.88	1.43	0.59
W3	1.23	1.48	0.67
W4	2.75	1.22	0.54
W4*	2.87	1.38	0.65
W5	1.47	1.45	0.46
W6	2.74	1.47	0.53

3.2. Erosion Mechanisms

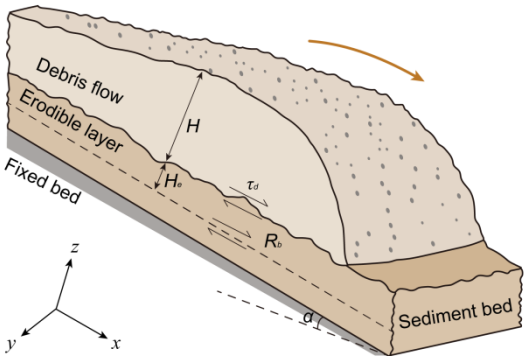

Figure 9. Schematic illustration of the equilibrium model during the erosion process.

As shown in Figure 9, the erosion model to analyze the erosion process consists of a debris flow layer with a free top surface, an erodible bed layer with a erodible basal boundary, and a fixed bed which cannot be eroded [*Iverson,* 2012; *Pudasaini and Krautblatter,* 2021]. Static equilibrium is reached when the total shear stress R_e exerted by the debris flow and the component of weight of the eroded sediment layer in the flow direction sum to the resistance stress R_b of the basal boundary. R_e is expressed as

$$R_e = \tau_d + \rho_b g H_e \sin\alpha \tag{2}$$

where ρ_b is the density of the bed sediment and H_e is the erosion depth. g is gravitational acceleration. The shear stress τ_d exerted on the debris flow is expressed as [*Pudasaini and Fischer,* 2020a; *Pudasaini and Krautblatter,* 2021]

$$\tau_d = \mu\left(\rho g H \cos\alpha - p_f\right) \tag{3}$$

where ρ is the flow-front density and H is the flow depth. μ is the Coulomb friction coefficient and p_f is the fluid stress in the debris flow.

The basal resistance R_b is given by

$$R_b = \left(\sigma - p\right)\tan\varphi + c \tag{4}$$

where σ is the bed normal stress, p is the pore pressure and $(\sigma–p)$ is the effective stress.

As physically modelled in *Pudasaini and Krautblatter* [2021], a comparison of

detailed sensor data indicates that erosion mechanisms induced significant differences in the erosion pattern and mean erosion rate of CBS and WBS. As shown in Figures 10 and 11, the black traces depict flow surface level $h(t)$, basal total normal stress $\sigma(t)$ and basal pore-fluid pressure $p(t)$ measured as the released flows C1, C2, C4 and C6 interacted with the bed sediment at x = 5.8 m [*Zheng,* 2021]. The red traces describe the analogous data from flows W1, W2, W4 and W6. Taking flows C2 and W2 as an example, flow C2 had a nose with a thick flow depth (8.9 cm) followed by rapid increases in σ. Then h and σ abruptly decreased, accompanied by significant bed erosion. Conversely, flow W2 had a low front (2.5 cm) and slight change in σ. The pore pressure p lagged behind h and σ, implying a pore-pressure transmission from the flow into the bed sediment. Flow C2 demonstrated an obvious increase in p to almost liquefy the CBS, while p increased mildly as flow W2 passed over the WBS. In addition, stepwise erosion was obvious for flows C4 and C6, indicated by the stepped decrease in h and σ (Figure 11). This erosion was also observed in the debris flows at the Illgraben catchment [*Berger et al.,* 2011].

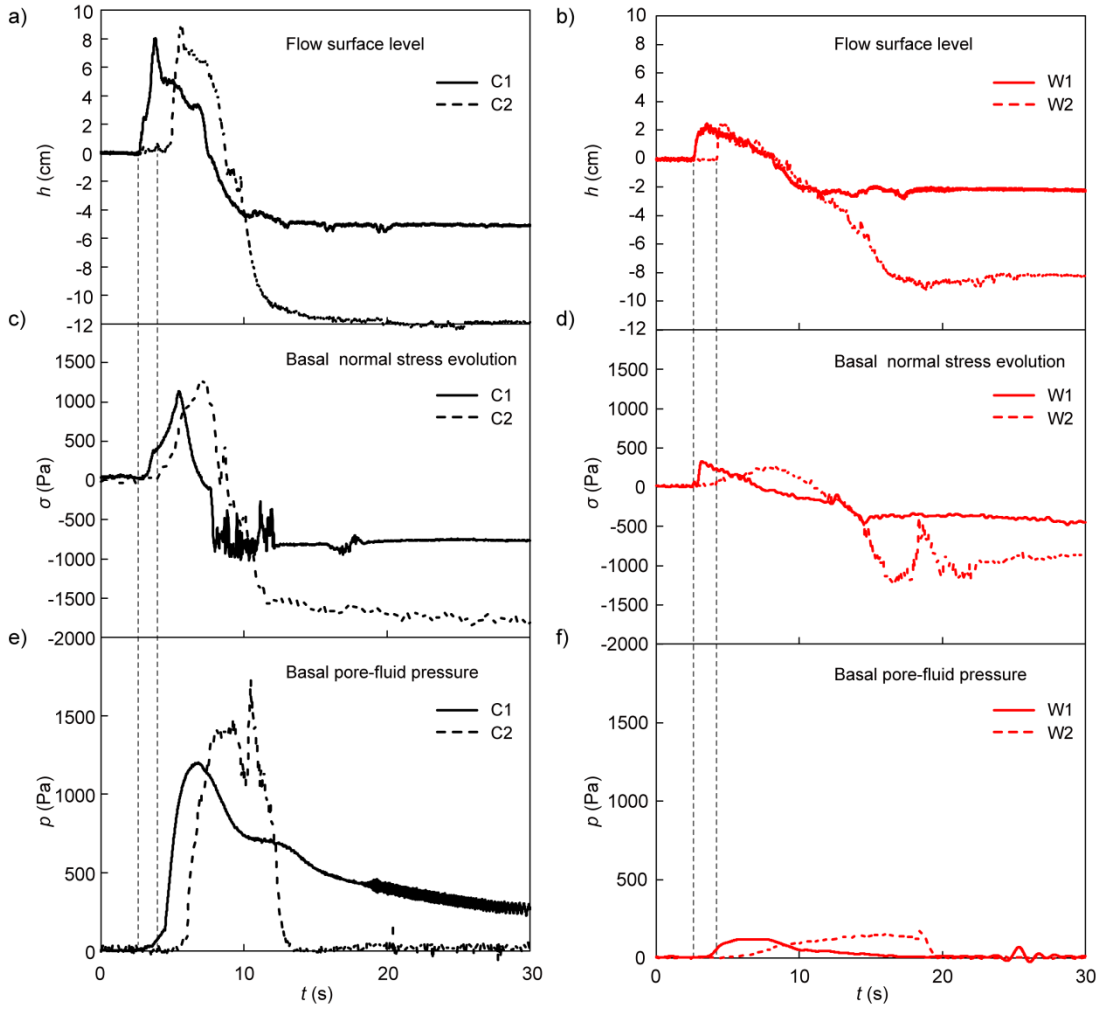

Figure 10. Time-series data acquired at x = 5.8 m in four experiments (flows C1, C2, W1 and W2)

with contrasting bed sediments. (a), (b), Sensor measurements of flow surface level $h(t)$, (c), (d), basal total normal stress $\sigma(t)$, and (e), (f), basal pore-fluid pressure $p(t)$. $\sigma(t)$ was the variation of the total normal stress induced by flow, not including the initial normal stress of the bed sediment.

The feedback effect of bed sediment on the erosion process strongly influenced flow behavior. When flows passed over the CBS, a nose of height 4.1–8.9 cm was maintained by substantial erosion of bed sediment (Figure 5). The pores in the flow and the bed became connected and significant pore-pressure transmission from the flow into the sediment bed occurred due to the high permeability coefficient (Figures 10 and 11). This brought about a decrease in the fluid pressure of the flow as a result of the unsaturated bed and consequently a significant decrease in the flow velocity [*Iverson et al.,* 2011; *de Haas and van Woerkom,* 2016]. Moreover, the high resistance of the nose was ascribed to large internal friction caused by continuous contact and slip among the frontal grains absent of surrounding fluid. The high resistance also tended to sustain a low velocity (0.41–0.66 m/s) of debris flow (Figure 4). Accordingly, flow behavior such as a high flow nose and low flow velocity were maintained on the CBS. Flow C1 had the lowest velocity (0.41 m/s) due to the high flow nose (7.8 cm) and limited released flow volume (0.04 m^3).

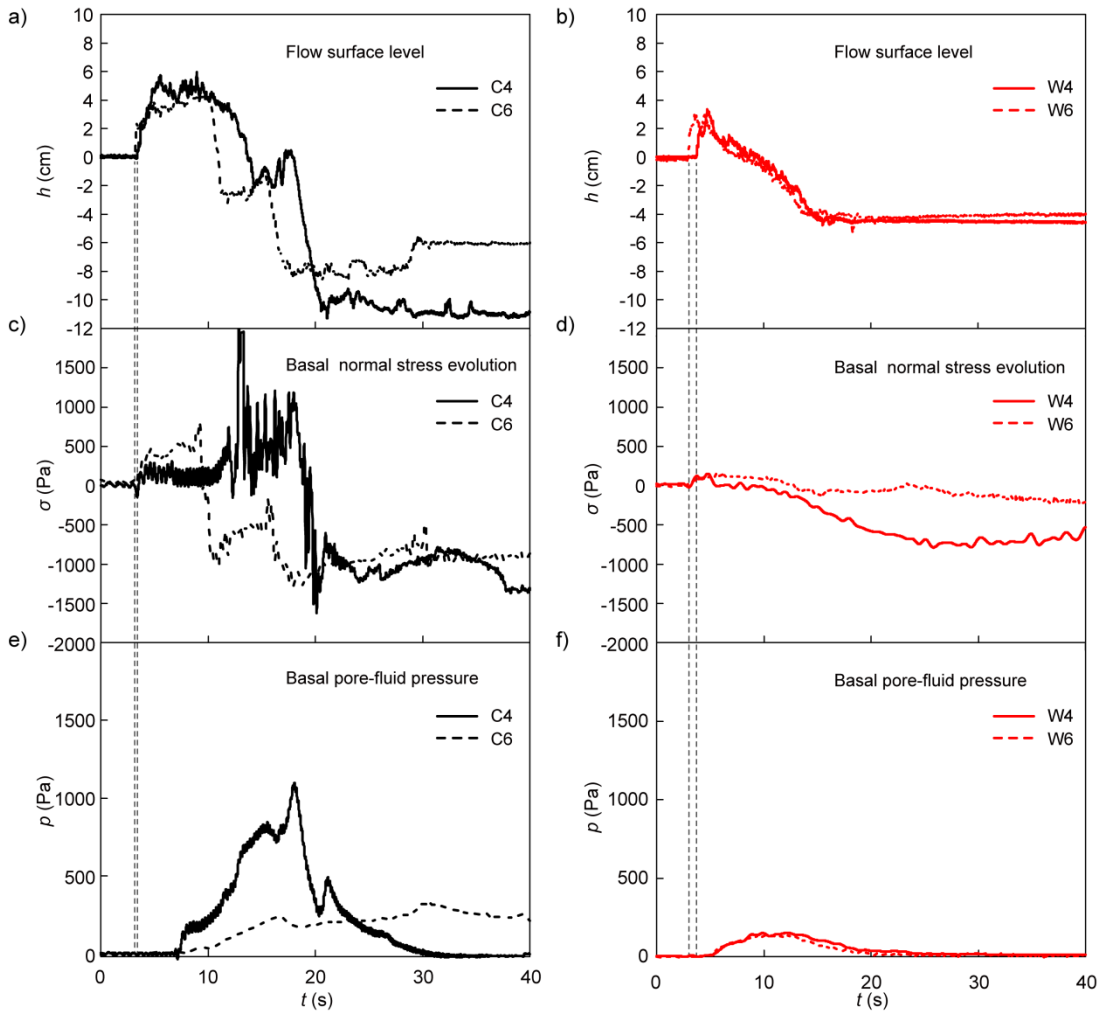

Figure 11. Time-series data acquired at x = 5.8 m in four experiments (flows C4, C6, W4 and W6) with contrasting bed sediments. (a), (b), Sensor measurements of flow surface level $h(t)$, (c), (d), basal total normal stress $\sigma(t)$, and (e), (f), basal pore-fluid pressure $p(t)$.

A tabular flow with a low height (2.3–3.3 cm) and a higher flow velocity (1.17–1.48 m/s) was developed on the WBS by gradually scouring bed sediment (Figures 4 and 5). On one hand, the fluid pressure in the debris flow was low due to the low flow height. The pore-pressure transmission from the flow into the bed sediment was limited as a result of the weak fluid pressure and low permeability coefficient of the WBS (Table 1). On the other hand, the decrease in flow velocity by bed erosion adding flow mass with zero velocity was small due to a low mean erosion rate. Thus, flow behavior such as low flow height and high flow velocity were maintained.

Flow behavior in turn significantly affected the erosion rate of bed sediment. The high flow nose on the CBS formed a mobile dam which tended to impede subsequent flow runout, leading to an increase in the flow depth H (Figure S2). The basal shear stress exerted on the bed by the moving flow was enhanced (Equation (3)). Moreover, the sustained high pore pressure (320–1660 Pa) significantly reduced the effective

stress and erosion resistance stress of the CBS (Equation (4)). In addition, the protrusion into the flow of the larger grains could enhance the drag force of the CBS [*Gregoretti,* 2008; *Recking,* 2009]. A layer of mass-movement grains was led by the flow nose, leading to a high q.

The tabular flow had a low flow depth and exerted a low basal shear stress on the WBS (Equation (3)). Pore pressure (80–180 Pa) was weak compared with the CBS. The effective stress and resistance stress were preserved during the process of erosion (Equation (4)). The surficial bed grains concentrated in the channel were progressively scoured away by the shear flow above, resulting in a low q.

The erosion depth H_e could be calculated from measured data. Considering the erosion process was dynamic, the maximum erosion depth was calculated from the maximum flow-front depth and pore pressure throughout the measurement. Taking flows W4 (W4*) and C4 (C4*) as an example, the flow density ρ was taken as 1700 kg/m^3, and flow depths H were 3 cm and 6 cm on the WBS and CBS, respectively. The pore pressures p were 180 Pa and 800 Pa for the WBS and CBS, respectively. Considering the flow-front velocity on the erosion zone of a sediment bed is nearly steady, the shear stress of debris flow is approximately equal to the stress applied by the downslope gravity [*Han et al.,* 2015; *de Haas and van Woerkom,* 2016]. The erosion depths H_e were 0.5 cm and 4.5 cm for the WBS and CBS, respectively, from Equation (2). This disparity is consistent with the experimental observation that the CBS was eroded by mass movement and the WBS was progressively scoured.

The interaction between the overlying flow and sediment bed during erosion is principally attributed to pore-pressure transmission. Debris flow and coarse-grained sediment were interconnected in the erosion process and capable of pressure transmission, while most air bubbles in pores were probably entrapped by surrounding fluid. Sustained high pore pressure in the bed sediment induced substantial erosion and a high flow nose, which in turn maintained the high pore pressure. By contrast, the transmission of pore pressure was weak between flow and widely graded sediment. This was partly caused by the low permeability. In addition, the air bubbles in pores were possibly difficult to expel during the erosion process [*Iverson et al.,* 2011].

4. Discussion

In this section, we discuss the effects of pore pressure and flow density on bed-sediment erosion, compare the experimental erosion pattern with debris flows measured in the field and in large-scale experiments, and show briefly the translation of these experimental results to natural systems.

4.1. Effects of Pore Pressure on Bed Sediment Erosion

A sensitivity analysis was performed to assess the effects of pore-pressure

variations on the erosion depths of the WBS and CBS using equilibrium analysis (Equations (2-4)). All the initial parameters were kept the same as for flows W4 and C4 but the pore pressure varied from -30% to 30%. Erosion could not occur if the calculated erosion depth was negative. As shown in Figure 12, the erosion depth varied linearly with pore pressure for the WBS and CBS. This is consistent with the observation of debris flows in the field [*Berger et al.,* 2011; *McCoy et al.,* 2012] and theoretical analysis [*Iverson,* 2012] that erosion rate is sensitive to pore pressure in the bed sediment. The erosion depths H_e were in the range 1.1–7.9 cm and 0–1.6 cm for the CBS and WBS, respectively. As a result of the high flow nose and pore pressure, the erosion-depth variation of the CBS with pore pressure was approximately three times that of the WBS.

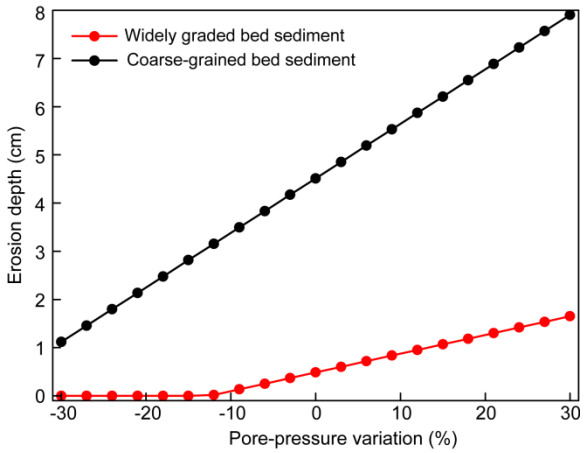

Figure 12. Sensitivity analysis of pore-pressure variation on the erosion depth.

The mean erosion rate increased with flow volume for the CBS whereas it was scarcely affected by flow volume for the WBS (Figure 8). As shown in Figure 13, the maximum flow depths of flows C1, C3 and C5 with released volumes of 0.04 m^3 were 7.8 cm, 5.9 cm and 4.1 cm, respectively. These were lower than the values for the corresponding flows C2 (C2*), C4 (C4*) and C6 with released volumes of 0.07 m^3. The maximum pore pressures of flows C1, C3 and C5 were 1390 Pa, 380 Pa and 200 Pa, respectively, which were enhanced for flows C2 (C2*), C4 (C4*) and C6. Compared with released flows of volume 0.07 m^3, flows of 0.04 m^3 on the CBS had a slightly lower flow depth at the front, and the basal shear stress and pore pressure were reduced. As a result, mean erosion rates were smaller for the released flows of volume 0.04 m^3 on the CBS than for flows of the same density with volumes of 0.07 m^3. By contrast, for each WBS, the maximum flow height was limited to 2.3–3.3 cm and pore pressure was merely 80–180 Pa, so q remained nearly the same for flows of different volumes because of progressive downward scour.

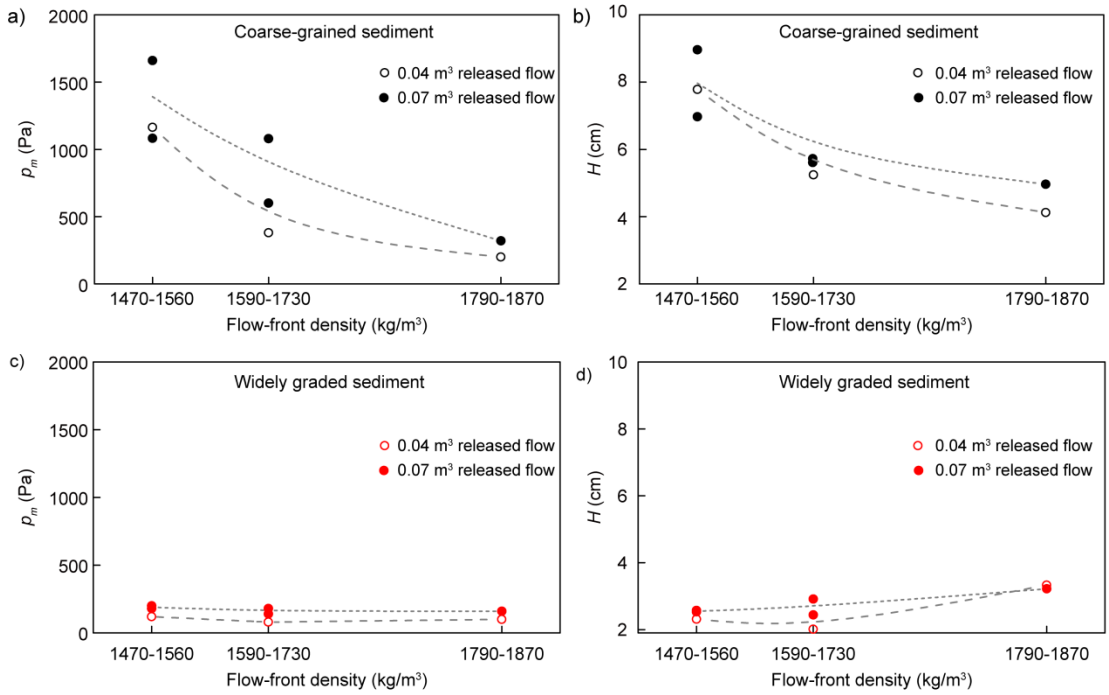

Figure 13. Maximum pore pressure p_m and flow depth H (at x = 5.8 m) during flow erosion.

The conspicuous effects of the pore pressure on changes in the erosion rate and erosion pattern raise a question about the mechanism of pore-pressure development. Pore pressure in the erodible bed originates from flow transmission and bed sediment. For the former, the fluid pressure of the flow could be translated into pore pressure in the bed sediment through downward transmission [*de Haas and van Woerkom,* 2016]. The fluid pressure can be higher than hydrostatic pressure by small volumetric contractions or grain collision of coarse debris, and persist due to the low permeability of debris-flow mixtures with slurry [*Iverson,* 2005; *Lanzoni et al.,* 2017]. For the latter, direct compression of pores by flow weight is probably responsible for pore-pressure changes in the bed sediment. Moreover, shear contraction of bed sediment in the loose state induced by moving debris flow can also increase pore pressure [*Iverson et al.,* 2000; *Iverson,* 2005].

The maximum pore pressure in the CBS decreased with flow-front density, while it was scarcely affected by flow-front density for the WBS (Figure 13). For the experimental debris flows presented here, the pore pressure in the erodible bed with a relatively low water content is mainly attributable to the flow pressure in the debris flow. The slurry volume decreased with increasing released flow density. Moreover, the flow depth at the front significantly decreased with flow-front density as a result of the erosion volume of the CBS (Figure 13). The maximum pore pressure was thus reduced with the flow pressure of debris flow. By contrast, flow depth at the front was merely 2.3–3.3 cm for different released flows on the WBS and the permeability coefficient of the bed sediment was low. The maximum pore pressure did not have an

obvious relationship with flow-front density.

4.2. Effects of Flow Density on Bed-Sediment Erosion

The mean erosion rate q had a negative correlation with flow-front density for the CBS under the same released volume, whereas q on the WBS initially increased with flow-front density and then decreased (Figure 8). As the flow-front density increased, flow nose height and pore pressure on the CBS were reduced (Figures 13a and 13b), leading to a lower basal shear stress and a higher basal resistance. For the WBS, the basal shear stress increased with flow-front density and thus q first increased. Thereafter, q decreased over the erodible bed area when the viscous slurry of flows W5 and W6 was deposited on the surface of the bed sediment (Figure S5).

We experimentally show that q decreased with flow-front density on the CBS. This trend is consistent with the findings of *Hungr et al.* [2005]. q on the WBS initially increased with flow-front density whereas the erosion rate decreased above a flow-front density of approximately 1700 kg/m^3. This is consistent with the experimental observation of *Rickenmann et al.* [2003]. The effect of flow density on the erosion rate can vary with the grain composition of bed sediment. The reason is that bed sediments with different grain compositions have a significant effect on the flow behavior and erosion pattern during erosion.

4.3. Erosion Patterns and Mobility

Our finding that the erosion pattern of the CBS was mass movement does not preclude the possibility that mass movement might exist in the WBS. In the experimental debris flows presented here, a flow nose developed in the erosion process of the CBS, which is similar to that of natural debris flow containing boulders [*Takahashi,* 2007]. According to *Iverson et al*. [2011], debris flows already having such a nose flowed across wet WBS. The flow nose was maintained and sustained high pore pressure generated as wet bed sediment was overridden, resulting in bed erosion by mass movement. This erosion process is consistent with that of the CBS in our experiments. Conversely, the flow nose gradually diminished and pore pressure increased minimally as the same debris flows flowed across dry WBS. The slurry of debris flow was gradually consumed in the dry sediment and pore pressure was weak which contributed to a low erosion rate.

Our experimental results show that the CBS with high shear strength has a greater mean erosion rate than the WBS with low shear strength. This seemingly contradictory conclusion is consistent with the observations of natural debris flows in Sedgwick Reserve and Acquabona [*Berti and Simoni,* 2005; *Gabet and Mudd,* 2006]. The reason is that the hydraulic conductivity of the CBS is high, contributing to a significant pore pressure developed in the CBS.

The flow velocity and mobility were reduced on the erodible beds for debris flows with different densities and volumes, compared with flows on the fixed bed upstream. This is consistent with experimental observations of *de Haas and van Woerkom* [2016]. However, debris flows grow in size and speed on wet bed sediment as reported by *Iverson et al.* [2011]. The reason for the difference may be that the saturation degree of bed sediments in our experiments is smaller than the values in *Iverson et al.* [2011]. As rigorously proven by *Pudasaini and Krautblatter* [2021], erosion and entrainment are mechanically fundamentally different processes: erosion results in entrainment, which in turn may lead to the enhanced mobility of mass movement when bed sediment is mechanically weaker than the flow itself. This is because the effective resistance of bed sediment is reduced, resulting in increased net momentum production of the flow [*Pudasaini and Krautblatter,* 2021].

4.4. Translation to Natural Flows

The flow behavior of our experimental debris flows was largely similar to that of natural debris flows. A high flow front, followed by more dilute material, developed on the CBS and tabular flow developed on the WBS which are typical characteristics of natural debris flows [e.g., *Liu and Huang,* 2006; *Iverson et al.,* 2010]. The erosion patterns of mass movement and progressive scour are consistent with the observation of debris flows in the field [*Berger et al.,* 2011; *McCoy et al.,* 2012; *McGuire et al.,* 2017] and in large-scale experiments [*Iverson et al.,* 2010]. In particular, stepwise erosion of flows C4 and C6 also occurred in the debris flows at the Illgraben catchment [*Berger et al.,* 2011]. The mean erosion rate of the CBS and WBS ranged from 0.3–1.8 cm/s, which is within the range of mean erosion rates (0.2–14.0 cm/s) for dry and wet bed sediments measured in Chalk Cliffs [*McCoy et al.,* 2012].

Dimensionless parameters estimated for natural debris flows and physical models were compared, in order to evaluate quantitatively the similarity in flow regimes of experimental and natural debris flows. Four dimensionless parameters – the Bagnold number N_{Bag}, Savage number N_{Sav}, Friction number N_{Fri}, and grain Reynolds number N_{Rg} – have been proposed to describe the relative importance of collisional, frictional, and viscous forces [*Iverson,* 1997; *Parsons et al.,* 2001; *Iverson and Denlinger,* 2001]. A debris flow tends to be dominated by grain collisions (inertial regime) when N_{Sav}>0.1 and collisional forces dominate over viscous forces for N_{Bag}>200 [*Bagnold,* 1954; *Savage and Hutter,* 1989; *Iverson and Denlinger,* 2001]. Frictional forces begin dominating viscous forces at N_{Fri}>250 for the debris flow front [*Parsons et al.,* 2001]. Generally, debris flows with respect to grains begin to show inertial effects and deviate significantly from ideal viscous behavior when N_{Rg}>1 [*Vanoni,* 1975]. The calculations of these dimensionless parameters see Text S1 in the

supplementary document.

As shown in Figure 14, collisional forces are dominated by viscous forces and frictional forces dominate over viscous forces for experimental flows during erosion. The debris flows on the WBS have a larger grain inertial effect than those on the CBS by comparing N_{Bag} and N_{Sav}, due to a higher flow velocity (Table 3). The effect of frictional forces becomes more important in the debris flows on the CBS than on the WBS by comparing N_{Fri} as a result of higher flow depth (Figure 13). The grain inertia always plays a more important role than the fluid inertia for all debris flows because of the interactions of dense debris grains.

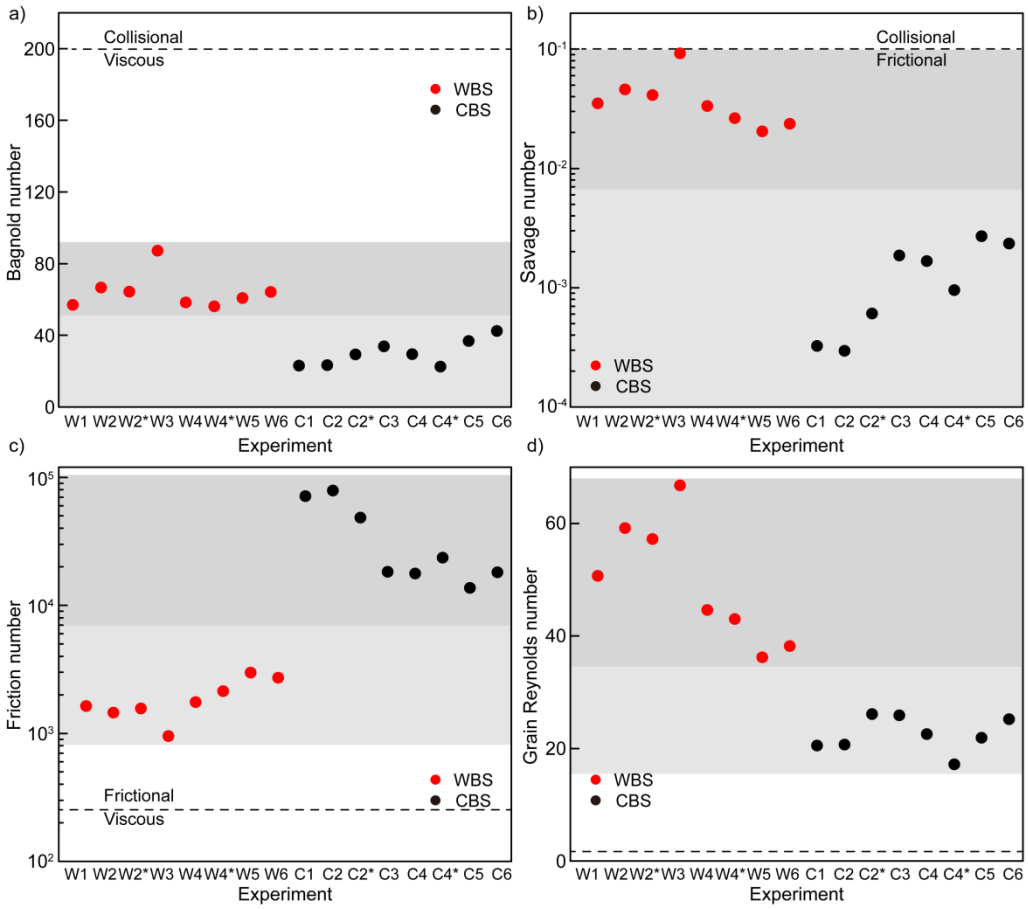

Figure 14. Effects of bed sediment on the flow regime: (a) Bagnold number; (b) Savage number; (c) friction number; (d) grain Reynolds number.

As shown in Table 4, the dimensionless numbers representing flow behavior for our experimental debris flows vary within the ranges of values that developed in the large-scale USGS flume and in natural debris flows [*Iverson,* 1997; *Iverson and Denlinger,* 2001; *Zhou and Ng,* 2010]. An uncertainty associated with the translation of our experimental results to natural debris flows is that bank collapse might fortify erosion volumes in natural debris-flow torrents. Whether our finding that the CBS (maximum grain size 5 mm) tends to be eroded by debris flow are suitable for natural boulders with median diameters up to tens of centimeters remains to be verified.

Table 4. Physical and dimensionless parameters estimated for the present laboratory experiments during erosion and large-scale, natural debris flows

Parameter	Symbol (Unit)	Present tests	USGS Flume Debris Flows [a]	Natural Debris Flows [a, b, c]
Typical grain diameter	d_s (m)	0.001–0.002	0.001	10^{-5}–10
Flow depth	H (m)	0.02–0.07	0.1	0.1–10
Flow shear rate	γ (1/s)	5–74	100	1–100
Solid density	ρ_s (kg/m^3)	2700	2700	2500–3000
Fluid density	ρ_f (kg/m^3)	1000–1207	1100	1000–1200
Solid volume fraction	C_v (–)	0.3–0.5	0.6	0.4–0.8
Fluid viscosity	μ_f (Pa s)	0.001–0.0015	0.001	0.001–0.1
Friction angle	ϕ (deg)	27–33	40	25–45
Savage number	N_{Sav}	0.0003–0.09	0.2	10^{-7}–10^{0}
Bagnold number	N_{Bag}	22–87	400	10^{0}–10^{8}
Friction number	N_{Fri}	950–78612	2000	10^{0}–10^{5}
Grain Reynolds number	N_{Rg}	17–67	100	0.01–2

[a]Iverson (1997).

[b]Iverson and Denlinger (2001).

[c]Zhou and Ng (2010).

5. Conclusions

We experimentally investigated the erosion of bed sediments by flows at a fixed to erodible bed transition. In particular, we calculated the erosion rates of coarse-grained (1–5 mm) bed sediment (CBS) and widely graded (0.01–5 mm) bed sediment (WBS), discerned erosion patterns and verified the proposed hypothesis of the interaction between overlying flow and bed sediments.

(1) Flow-front velocity slightly decreased on a WBS, whereas a significant reduction in flow-front velocity occurred on a CBS. A high flow nose developed when the debris flow moved across the CBS, but a tabular flow developed on the WBS.

(2) The distribution of erosion depth on the CBS was relatively uniform in the cross-stream direction. Driven by the nose, the CBS was eroded by a layer of mass movement. A strip of channelized erosion developed on the WBS. Surficial sediment was eroded by progressively scouring bed sediments. The CBS generally had a greater mean erosion rate than the WBS for the same released flow.

(3) The feedback effect of bed sediment on the erosion process strongly influenced flow height and velocity, which in turn affected the mean erosion rate of bed sediment. The interaction between debris flow and a sediment bed during erosion is principally attributed to pore-pressure transmission.

(4) The mean erosion rate increased with flow volume and decreased with the increase of flow-front density for the CBS. However, the mean erosion rate was scarcely affected by flow volume for the WBS and initially increased with flow-front density and then decreased.

These results suggest that grain composition of bed sediment has a significant influence on the debris-flow characteristics and erosion pattern during the erosion. Further research will focus on the erosion process of debris flow on beds with different slopes. The data obtained from these experiments can serve in further validating other experiments and the multi-mechanical, multi-phase, mass flow models [*Rosatti and Begnudelli,* 2013; *Cuomo et al.,* 2016; *Gregoretti et al.,* 2019; *Pudasaini and Mergili,* 2019] that have already been applied to many complex natural flows including the bed erosion process.

Acknowledgements

We thank the State Key Laboratory of Geohazard Prevention and Geoenvironment Protection in China for offering the experimental site and apparatus, and we acknowledge funding from the Natural Science Foundation of China (No. 42007252 and 41731283). Constructive reviews by the associate editor and five anonymous reviewers helped to improve the manuscript and are gratefully acknowledged. We note all of the data in the present work are available online at https://doi.org/10.5281/zenodo.5533099.

References

Abancó, C., and M. Hürlimann (2014), Estimate of the debris-flow entrainment using field and topographical data, *Nat. Hazards, 71,* 363–383.

Bagnold, R. A (1954), Experiments on a gravity-free dispersion of large solid spheres in a Newtonian fluid under shear, *Proc. R. Soc. A, 225 (1160),* 49–63.

Berger, C., B. W. McArdell, B. Fritschi, and F. Schlunegger (2010), A novel method for measuring the timing of bed erosion during debris flows and floods, *Water Resour. Res., 46,* W02502.

Berger, C., B. McArdell, and F. Schlunegger (2011), Direct measurement of channel erosion by debris flows, Illgraben, Switzerland, *J. Geophys. Res.-Earth Surf., 116,* F01002.

Berti, M., R. Genevois, A. Simoni, and P. R. Tecca (1999), Field observations of a debris flow event in the Dolomites, *Geomorphology, 29(3-4),* 265–274.

Berti, M., and A. Simoni (2005), Experimental evidences and numerical modelling of debris flow initiated by channel runoff, *Landslides, 2,* 171–182.

Boreggio, M., M. Bernard, and C. Gregoretti (2018), Evaluating the differences of gridding techniques for digital elevation models generation and their influence on the modeling of stony debris flows routing: a case study from Rovina di Cancia Basin (North-Eastern Italian Alps), *Front. Earth Sci., 6,* 89.

Breien, H., F. V. De Blasio, A. Elverhøi, and K. Høeg (2008), Erosion and morphology of a debris flow caused by a glacial lake outburst flood, western Norway, *Landslides, 5,* 271–280.

Chen, J., Y. He, and F. Wei (2005), Debris flow erosion and deposition in Jiangjia Gully, Yunnan, China, *Eng. Geol., 48,* 771–777.

Chen, H. X., and L. M. Zhang (2015), EDDA 1.0: integrated simulation of debris flow erosion, deposition and property changes, *Geosci. Model Dev., 8(3),* 829–844.

Conway, S., A. Decaulne, M. Balme, J. Murray, and M. Towner (2010), A new approach to estimating hazard posed by debris flows in the Westfjords of Iceland, *Geomorphology, 114,* 556–572.

Costa, J. E. (1988), Rheologic, geomorphic, and sedimentologic differentiation of water flood, hyperconcentrated flows, and debris flows, in Flood Geomorphology, chap. Rheologic, geomorphic, and sedimentologic differentiation of water floods, hyperconcentrated flows, and debris flows, pp. 113–122, John Wiley, New York.

Cuomo, S., M. Pastor, V. Capobianco, and L. Cascini (2016), Modelling the space-time bed entrainment for flow-like landslide, *Eng. Geol., 212,* 10–20.

de Haas, T., and T. van Woerkom (2016), Bed scour by debris flows: experimental investigation of effects of debris-flow composition, *Earth Surf. Proc. Landf., 41,* 1951–1966.

Dong, J. J., Y. Li, C. Kuo, R. Sung, M. Li, C. Lee, C. Chen, and W. Lee (2011), The formation and breach of a short-lived landslide dam at Hsiaolin village, Taiwan—part I: post-event reconstruction of dam geometry, *Eng. Geol., 123,* 40-59.

Dowling, C. A., and P. M. Santi (2014), Debris flows and their toll on human life: a global analysis of debris-flow fatalities from 1950 to 2011, *Nat. Hazards, 71,* 203–227.

Fan, X., G. Scaringi, O. Korup, A. Joshua West, C. J. van Westen, H. Tanyas, N. Hovius, T. C. Hales, R. W. Jibson, K. E. Allstadt, L. Zhang, S. G. Evans, C. Xu, G. Li, X. Pei, Q. Xu, and R. Huang (2019), Earthquake-induced chains of geologic hazards: Patterns, mechanisms, and impacts, *Rev. Geophys., 57,* 421–503.

Gabet, E. J., and S. M. Mudd (2006), The mobilization of debris flows from shallow landslides, *Geomorphology, 74,* 207–218.

Gregoretti, C. (2000), The initiation of debris flow at high slopes: Experimental results, *J. Hydraul. Res., 38,* 83–88.

Gregoretti, C. (2008), Inception sediment transport relationships at high slope, *J. Hydraul. Eng., 134 (11),* 1620–1629.

Gregoretti, C., M. Degetto, M. Bernard, and M. Boreggio (2018), The debris flow occurred at Ru Secco Creek, Venetian Dolomites, on 4 August 2015: analysis of the phenomenon, its characteristics and reproduction by models, *Front. Earth Sci., 10,* 3389.

Gregoretti, C., M. L. Stancanelli, M. Bernard, M. Boreggio, M. Degetto, and S. Lanzoni (2019), Relevance of erosion processes when modelling in-channel gravel debris flows for efficient hazard assessment, *J. Hydrol.,* 569, 575–591.

Guthrie, R., A. Hockin, L. Colquhoun, T. Nagy, S. Evans, and C. Ayles (2010), An examination of controls on debris flow mobility: evidence from coastal British Columbia, *Geomorphology, 114,* 601–613.

Han, Z., G. Chen, Y. Li, and Y. He (2015), Assessing entrainment of bed material in a debris-flow event: a theoretical approach incorporating Monte Carlo method, *Earth Surf. Processes Landforms, 40,* 1877–1890.

Houghton, J. T., Y. Ding, D. J. Griggs, M. Noguer, P. J. van der Linden, X. Dai, K. Maskell, and C. A. Johnson (2001), *Climate Change 2001: The Scientific Basis,* Cambridge Univ. Press, London.

Hsu, L., W. E. Dietrich, and L. S. Sklar (2008), Experimental study of bedrock erosion by granular flows, *J. Geophys. Res.-Solid Earth, 113,* F02001.

Hungr, O., S. McDougall, and M. Bovis (2005), Entrainment of material by debris flows. In Debris-Flow Hazards and Related Phenomena, (Ed. Jakob, M., & Hungr, O.), pp. 135–158, Springer, Berlin.

Iverson, R. M. (1997), The physics of debris flows, *Rev. Geophys., 35(3),* 245–296.

Iverson, R. M., M. E. Reid, N. R. Iverson, R. G. LaHusen, M. Logan, J. E. Mann, and D. L. Brien (2000), Acute sensitivity of landslide rates to initial soil porosity, *Science, 290,* 513–516.

Iverson, R. M. (2005), Regulation of landslide motion by dilatancy and pore-pressure feedback, *J. Geophys. Res.,* 110, F02015.

Iverson, R. M., and R. P. Denlinger (2001), Flow of variably fluidized granular masses across three-dimensional terrain: 1. Coulomb mixture theory, *J. Geophys. Res. 106 (B1),* 537–552.

Iverson, R. M., M. Logan, R. G. LaHusen, and M. Berti (2010), The perfect debris flow? Aggregated results from 28 large-scale experiments, *J. Geophys. Res., 115,* F03005.

Iverson, R. M., M. E. Reid, M. Logan, R. G. LaHusen, J. W. Godt, and J. P. Griswold (2011), Positive feedback and momentum growth during debris-flow entrainment of wet bed sediment, *Nature Geosci., 4,* 116–121.

Iverson, R. M. (2012), Elementary theory of bed-sediment entrainment by debris flows and avalanches, *J. Geophys. Res.-Earth Surf., 117,* F03006.

Jakob, M., O. Hungr, and D. M. Jakob (2005), in *Debris-Flow Hazards and Related Phenomena* (eds Jakob, M. & Hungr, O.) 135–158, Springer, Chichester.

Lanzoni, S., C. Gregoretti, and L. M. Stancanelli (2017), Coarse-grained debris flow dynamics on erodible beds, *J. Geophys. Res. Earth Surf.,* 122, 592–614.

Liu, K. F., and M. C. Huang (2006), Numerical simulation of debris flow with application on hazard area mapping, *Comput. Geosci., 10(2),* 221–240.

Mangeney, A. (2011), Geomorphology: Landslide boost from entrainment, *Nature Geosci., 4,* 77.

McCoy, S. W., J. W. Kean, J. A. Coe, G. E. Tucker, D. M. Staley, and T. A. Wasklewicz (2012), Sediment entrainment by debris flows: In situ measurements from the headwaters of a steep catchment, *J. Geophys. Res.–Earth Surf., 117,* F03016.

McGuire, L. A., F. K. Rengers, J. W. Kean, and D. M. Staley (2017), Debris flow initiation by runoff in a recently burned basin: Is grain-by-grain sediment bulking or en masse failure to blame?, *Geophys. Res.Lett., 44,* 7310–7319.

Navratil, O., F. Liébault, H. Bellot, E. Travaglini, J. Theule, G. Chambon, and D. Laigle (2013), High-frequency monitoring of debris-flow propagation along the Réal Torrent, Southern French Prealps, *Geomorphology, 201,* 157–171.

Parsons, J. D., K. X. Whipple, and A. Simoni (2001), Experimental study of the grain-flow, fluid-mud transition in debris flows, *Geology 109 (4),* 427–447.

Pérez, F. L. (2001), Matrix granulometry of catastrophic debris flows (December 1999) in central coastal Venezuela, *Catena, 45,* 163–183.

Pierce, J. L., G. A. Meyer, and A. J. T. Jull (2004), Fire-induced erosion and millennial-scale climate change in northern ponderosa pine forests, *Nature, 432,* 87–90.

Pierson, T. C. (1980), Erosion and deposition by debris flows at Mt. Thomas, North Canterbury, New Zealand, *Earth Surf. Processes, 5,* 227–247.

Pudasaini, S. P. (2012), A general two-phase debris flow model, *J. Geophys. Res.- Earth Surface, 117,* F03010.

Pudasaini, S. P., and M. Mergili (2019), A multi-phase mass flow model, *J. Geophys. Res.–Earth Surf.,* 124, 2920–2942.

Pudasaini, S. P., and J. T. Fischer (2020a), A mechanical erosion model for two-phase mass flows, *Int. J. Multiph. Flow, 132,* 103416.

Pudasaini, S. P., and J. T. Fischer (2020b), A mechanical model for phase separation in debris flow, *Int. J. Multiph. Flow 129,* 103292.

Pudasaini, S. P., and M. Krautblatter (2021), The mechanics of landslide mobility with erosion, *Nat Commun., 12,* 6793.

Quan Luna, B., A. Remaître, T. W. van Asch, J. P. Malet, and C. J. Van Westen (2012), Analysis of debris flow behavior with a one dimensional run-out model incorporating entrainment, *Eng. Geol., 128,* 63–75.

Recking, A. (2009), Theoretical development on the effect of changing flow hydraulics on incipient bed load motion, *Water Resour. Res.,* 45, W04401.

Reid, M. E., J. A. Coe, and D. L. Brien (2016), Forecasting inundation from debris flows that grow volumetrically during travel, with application to the Oregon Coast Range, USA, *Geomorphology, 273,* 396–411.

Rickenmann, D., D. Weber, and B. Stepanov (2003), Erosion by debris flows in field and laboratory experiments, In: Debris-Flow Hazards Mitigation–Mechanics, Prediction and Assessment (Ed. Rickenmann, D. and C. L. Chen), pp. 883–894, Millpress, Rotterdam, Padua.

Rosatti, G., and L. Begnudelli (2013), Two dimensional simulations of debris flows over mobile beds: Enhancing the TRENT2D model by using a well-balanced generalized Roe-type solver, *Comput. Fluids, 71,* 179–185.

Santi, P. M., J. D. Higgins, S. H. Cannon, and J. E. Gartner (2008), Sources of debris flow material in burned areas, *Geomorphology, 96,* 310–321.

Savage, S. B, and K. Hutter (1989), The motion of a finite mass of granular material down a rough incline, *J. Fluid Mech., 199,* 177–215.

Schürch, P., A. Densmore, N. Rosser, and B. W. McArdell (2011), A novel debris-flow fan evolution model based on debris flow monitoring and lidar topography, In: Fifth International Conference on Debris-Flow Hazards Mitigation–Mitigation, Mechanics, Prediction and Assessment (Ed. R. Genevois, D.L. Hamilton and A. Prestininzi), pp. 263–272, Casa Editrice Università La Sapienza, Padua.

Shi, Z., H. Zheng, S. Yu, M. Peng, and T. Jiang (2018), Application of CFD-DEM to investigate seepage characteristics of landslide dam materials, *Comput. Geotech., 101,* 23–33.

Simoni, A., M. Bernard, M. Berti, M. Boreggio, S. Lanzoni, L. M. Stancanelli, and C. Gregoretti (2020), Runoff-generated debris flows: Observation of initiation conditions and erosion–deposition dynamics along the channel at Cancia (eastern Italian Alps), *Earth Surf. Processes,* 45*,* 3556–3571.

Stock, J. D., and W. E. Dietrich (2006), Erosion of steepland valleys by debris flows, *Geol. Soc. Am. Bull., 118,* 1125–1148.

Stoffel, M., D. Tiranti, and C. Huggel (2014), Climate change impacts on mass movements — Case studies from the European Alps, *Sci. Total Environ., 493,* 1255–1266.

Suwa, H., K. Okano, and T. Kanno (2009), Behavior of debris flows monitored on test slopes of Kamikamihorizawa Creek, Mount Yakedake, Japan, *Int. J. Erosion Control Eng*., *2,* 33–45.

Takahashi, T., H. Nakagawa, T. Harada, and Y. Yamashiki (1992), Routing debris flows with particle segregation, *J. Hydraul. Eng., 118,* 1490–1507.

Takahashi, T. (2007), *Debris Flows: Mechanics, Prediction and Countermeasures, Proc. Monogr. Eng. Water Earth Sci.,* Taylor and Francis, Leiden.

Theule, J., F. Liébault, D. Laigle, A. Loye, and M. Jaboyedoff (2015), Channel scour and fill by debris flows and bedload transport, *Geomorphology, 243,* 92–105.

Tiranti, D., S. Bonetto, and G. Mandrone (2008), Quantitative basin characterisation to refine debris-flow triggering criteria and processes: an example from the Italian Western Alps, *Landslides, 5(1),* 45–57.

Vanoni, V. A (1975), Sedimentation Engineering, *Am. Soc. of Civil Eng.,* New York.

Wang, G., K. Sassa, and H. Fukuoka (2003), Downslope volume enlargement of a debris slide–debris flow in the 1999 Hiroshima, Japan, rainstorm, *Eng*. *Geol*., *69,* 309–330.

Yohannes, B., L. Hsu, W. Dietrich, and K. Hill (2012), Boundary stresses due to impacts from dry granular flows, *J. Geophys. Res.–Earth Surf.,117,* F02027.

Zheng, H., Z. Shi, M. Peng, and S. Yu (2018), Coupled CFD-DEM model for the direct numerical simulation of sediment bed erosion by viscous shear flow, *Eng. Geol., 245,* 309–321.

Zheng, H., Z. Shi, K. J. Hanley, M. Peng, S. Guan, S. Feng, and K. Chen (2021), Deposition characteristics of debris flows in a lateral flume considering upstream entrainment, *Geomorphology,* doi: 10.1016/j.geomorph.2021.107960.

Zheng, H. (2021), Supplementary Information for "Erosion mechanisms of debris flow on the sediment bed ", Zenodo, https://doi.org/10.5281/zenodo.5533099.

Zhou, G. G., and C. W. Ng (2010), Dimensional analysis of natural debris flows, *Can. Geotech. J., 47 (7),* 719–729.

Supplementary Information for "Erosion mechanisms of debris flow on the sediment bed"

Hongchao Zheng[1], Zhenming Shi[1], Songbo Yu[1]*, Xuanmei Fan[2]*, Kevin J Hanley[3], Shijin Feng[1]

[1]Key Laboratory of Geotechnical and Underground Engineering of the Ministry of Education, and Department of Geotechnical Engineering, College of Civil Engineering, Tongji University, China

[2]State Key Laboratory of Geohazard Prevention and Geoenvironment Protection, Chengdu University of Technology, China

[3]School of Engineering, Institute for Infrastructure and Environment, The University of Edinburgh, United Kingdom

Contents:

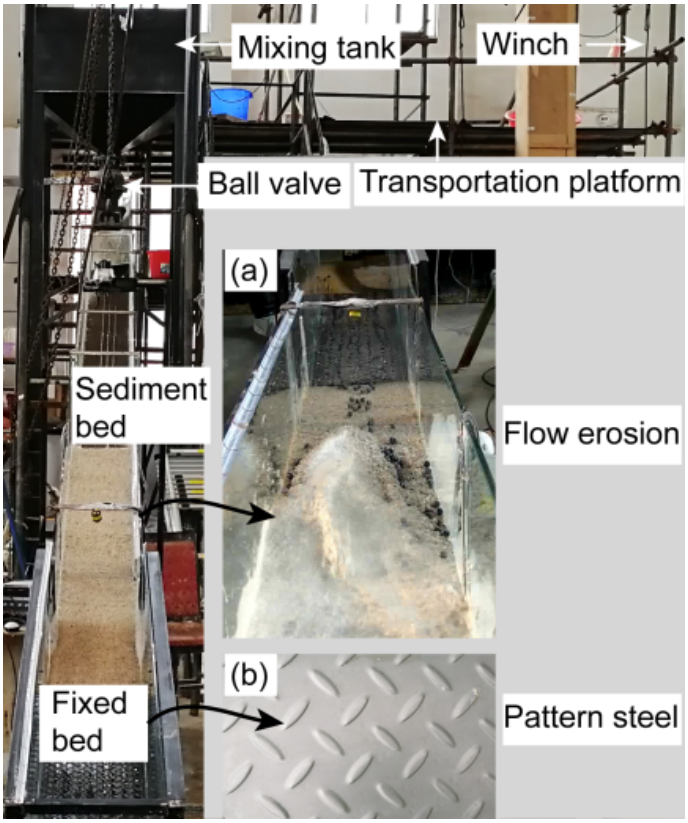

Figure S1. Experimental apparatus of debris-flow erosion. Inset photo (a) shows the flow nose of flow C4 encountering coarse-grained bed sediment. Inset photo (b) is the pattern steel on the fixed bed.

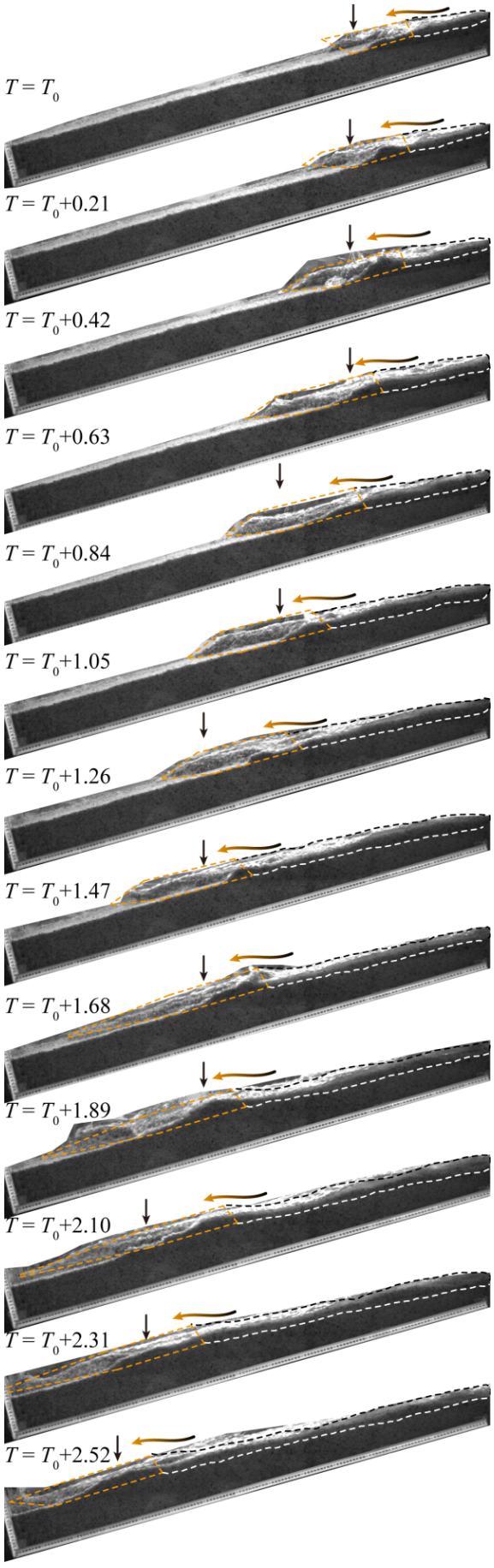
$T = T_0$
$T = T_0$+0.21
$T = T_0$+0.42
$T = T_0$+0.63
$T = T_0$+0.84
$T = T_0$+1.05
$T = T_0$+1.26
$T = T_0$+1.47
$T = T_0$+1.68
$T = T_0$+1.89
$T = T_0$+2.10
$T = T_0$+2.31
$T = T_0$+2.52

Figure S2. Erosion process of coarse-grained sediment by flow C2 (x = 4.2–5.8 m). The flow nose is located in the dashed orange box and the flow body is located in the black and white dashed box. The flow nose was higher than the flow body. The flow nose moved downstream, pushed by the following flow body. The coarse-grained sediment behind the flow nose was entrained by a layer of mass movement above the white dotted line. T_0 is the time corresponding to the first frame. The number of frames between two successive snapshots is 38 and the time interval is 0.21 s.

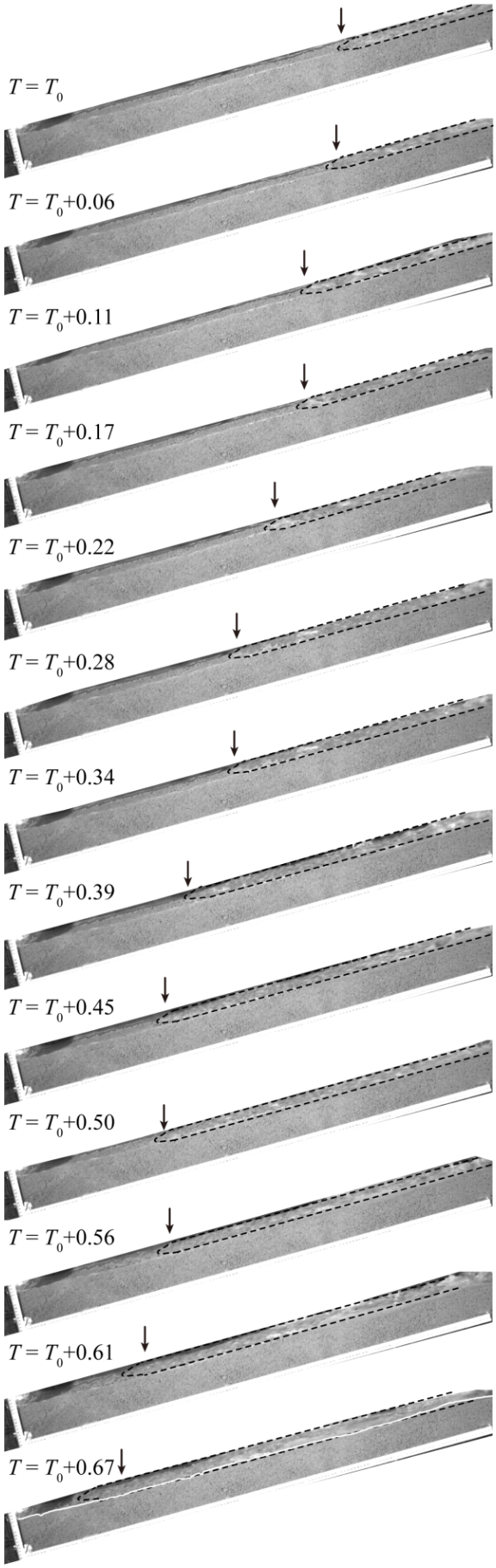
$T = T_0$
$T = T_0$+0.06
$T = T_0$+0.11
$T = T_0$+0.17
$T = T_0$+0.22
$T = T_0$+0.28
$T = T_0$+0.34
$T = T_0$+0.39
$T = T_0$+0.45
$T = T_0$+0.50
$T = T_0$+0.56
$T = T_0$+0.61
$T = T_0$+0.67

Figure S3. Erosion process of widely graded sediment by flow W2 (x = 4.2–5.8 m). Debris flow is located in the black dashed box. The flow height and velocity from the flow front to flow body did not display a significant change. The flow height was significantly smaller than that of flow C2. The white line at $T= T_0$+0.67 marks the boundary of the sediment bed before erosion. T_0 is the time corresponding to the first frame. The number of frames between two adjacent snapshots is 10 and the time interval is 0.056 s.

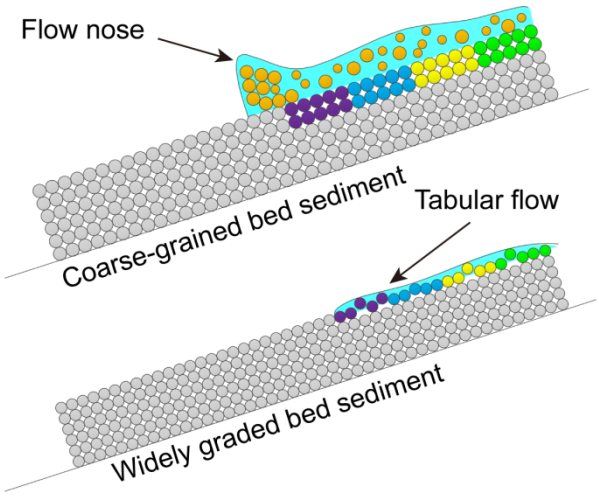

Figure S4. Schematic diagram of flows on the coarse-grained and widely graded bed sediments. A high flow nose developed when the debris flow moved over the coarse-grained bed sediment, while a tabular flow with a low flow height moved on the widely graded bed sediment.

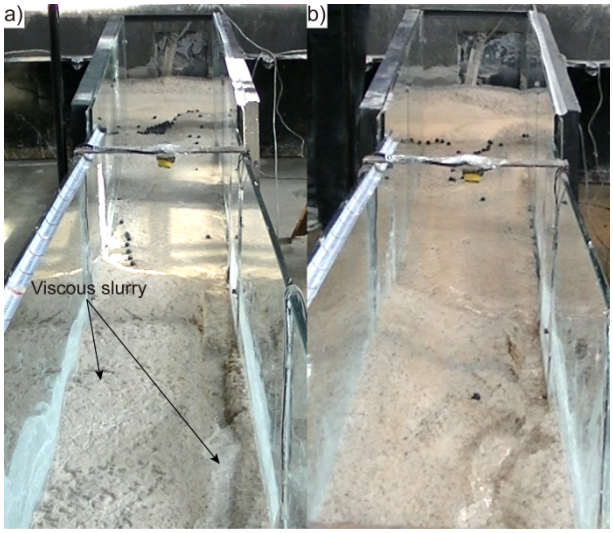

Figure S5. Widely graded bed sediment after erosion for (a) W6 and (b) W4. Photographs look from the sediment bed upstream. A sheet of viscous slurry was observed to be deposited on the surface of W6, whereas this did not occur on the surface of W4.

Text S1

Dimensionless parameters estimated for natural debris flows and physical models are compared, in order to evaluate quantitatively the similarity in flow regimes of experimental and natural debris flows. The following dimensional quantities at the flow front on the development zone have been considered to derive these dimensionless parameters: flow depth H, volume concentration C_v, grain density ρ_s, mean diameter d_s of the debris sediment, slurry density ρ_f, slurry viscosity μ_f and mean flow velocity v.

Collisional, frictional, and viscous forces are considered to resist motion in debris flows (Iverson, 1997; Parsons et al., 2001; Iverson and Denlinger, 2001). Inertial forces result from short-term collisions between sediment grains, frictional forces are related to continuous contacts between grains, and viscous forces are controlled by the slurry viscosity. Three dimensionless parameters describe the relative importance of these forces. The Savage number N_{Sav} describes the ratio of collisional to frictional forces,

$$N_{Sav} = \frac{\rho_s d_s^2 \gamma^2}{\left(\rho_s - \rho_f\right) gH \tan\varphi} \tag{S1}$$

where φ is the internal angle of friction.

The Bagnold number N_{Bag} defines the ratio of collisional to viscous forces,

$$N_{Bag} = \frac{C_v \rho_s \gamma d_s^2}{\left(1 - C_v\right) \mu_f} \tag{S2}$$

where γ is the flow shear rate (1/s),

$$\gamma = \frac{v}{H} \tag{S3}$$

The interstitial fluid viscosity μ_f was estimated as (Iverson, 1997)

$$\mu_f / \mu_w = 1 + 2.5C_{vf} + 10.05C_{vf}^2 + 0.00273\exp\left(16.6C_{vf}\right) \tag{S4}$$

where μ_w is the dynamic viscosity of pure water (0.001 Pa s) and C_{vf} is the volume fraction of the interstitial fluid occupied by the fine component.

The friction number N_{Fri} defines the ratio of frictional to viscous forces,

$$N_{Fri} = \frac{C_v \left(\rho_s - \rho_f\right) gH \tan\varphi}{\left(1 - C_v\right) \gamma \mu_f} \tag{S5}$$

The effects of particle collisions and slurry viscosity could be indicated by the grain Reynolds number N_{Rg} (Iverson, 1997), which is defined as the ratio between the solid inertial stress and the fluid viscous shearing stress:

$$N_{Rg} = \frac{\rho_f \gamma d_s^2}{\mu_f} \tag{S6}$$